Effect of chamber pressure on defect generation and their influence on corrosion and tribological properties of HIPIMS deposited CrN/NbN Coatings

Barnali Biswas [a,1], Y. Purandare [1], A. Sugumaran [1], Imran Khan [2] and Papken Eh. Hovsepian [1]

[1]National HIPIMS Technology Centre, Materials and Engineering Research Institute, Sheffield Hallam University, City Campus, Howard Street, Sheffield S1 1WB, United Kingdom

[2]Zimmer-Biomet UK Limited, Dorcan Industrial Estate, Murdoch Road, Swindon SN3 5HY, United Kingdom

[a)] Corresponding author: Barnali.Biswas@student.shu.ac.uk

Abstracts: It has been reported that compared to state-of-the-art technologies, High Power Impulse Magnetron Sputtering produces very dense and droplet free coatings due to the high plasma density and ionisation rate. However, thorough investigation of the coating morphology by Scanning Electron Microscopy, optical microscopy and other surface analysis methods revealed the existence of various types of coating defects.

This study reports the influence of chamber pressure in particular on defect formation in CrN/NbN nanoscale multilayer coatings. The coating series was deposited using combined HIPIMS/UBM technique while varying the total chamber pressure from 0.2 Pa to 1 Pa. Four types of defects were identified, namely, nodular, open void, cone-like and pinhole. Defect density calculations showed that the coating produced at the lowest pressure, 0.2 Pa, had the lowest defect density of 0.84%.

As expected coating corrosion properties improved linearly with decreasing defect density. Potentiodynamic polarisation corrosion studies revealed that in the potential range of - 300 mV to + 300 mV, the current density decreased with decreasing defect density (from 5.96% to 0.84%). In contrast, pin-on-disk tribology tests at room temperature demonstrated that the tribological properties of the coatings deposited at different chamber pressures were dependent on the crystallographic orientations and on the nature of the oxides formed at the

tribological contact. Coatings with (200) crystallographic orientation had lower wear rates (~ 1.6×10^{-15} $m^3N^{-1}m^{-1}$) whereas coating with (111) crystallographic orientation had the highest wear rate (2.6×10^{-15} $m^3N^{-1}m^{-1}$). Friction properties were influenced by the tribolayer formed during the tribological tests.

However, for the coatings deposited at same chamber pressure of 0.35 Pa but with different defect densities (due to the difference in chamber cleanliness), the friction behaviour was directly influenced by the coating defects. The friction co-efficient (μ) decreased by a factor of two from 0.48 to 0.25 when the defect density decreased from 3.18% to 1.37%.

1. Introduction:

Physical vapour deposited (PVD) hard transition metal nitride coatings have been successfully used for industrial applications. CrN, TiN and NbN coatings especially have shown notable protective properties against corrosion and wear [1–3]. Moreover, it has been reported that multilayer nitride coatings deposited by reactive magnetron sputtering can improve coating properties. For example TiN/VN and TiN/NbN multilayer coatings have shown high coating hardness whereas, TiN/CrN and CrN/NbN both have improved corrosion resistance and reduced wear rates due to their multilayer structures [4–7].

Recently, new generation PVD technique High Power Impulse Magnetron Sputtering (HIPIMS) has been used for depositing multilayer CrN/NbN coatings. Due to its high plasma density and ionisation rate, HIPIMS has been found to be effective in producing very dense coatings compared to state-of-the-art technologies [8–10]. Nevertheless, HIPIMS can produce homogeneous coatings on complex-shaped substrates which is not achievable by conventional sputtering deposition due to its anisotropic deposition flux [11]. Due to the denser microstructure and smaller grain size, HIPIMS deposited coatings exhibited lower surface roughness, higher hardness, improved adhesion, excellent wear and corrosion resistance [12–14]. Although the deposition rate during the HIPIMS process is quite low, this drawback can be eradicated by combining HIPIMS with the Unbalanced Magnetron Sputtering (UBM) process [15].

Additionally, previous research revealed that HIPIMS generated plasma is free from the droplet phase [8–10,15,16]. For the HIPIMS process, applied power is not constant; rather HIPIMS is associated with a pulsed power supply where the peak power exceeds the average power by typically two orders of magnitude [10]. The supply of immense high power in very short pulses (impulse) enhances the generation of metal ions (M^+) and the lower average

power prevents droplet formation. Thus, the deposited coatings can be free from droplet related defects.

However, detailed morphological investigation of HIPIMS coatings still shows some nanostructured defects. Any kind of growth defects are undesirable as these can restrain the coating functionality [17–22]. It can affect the surface roughness and surface finish, thus the tribological performance of the coatings can also be affected [18,19]. Nevertheless coating defects like pores, holes and voids can expose the substrate material to the corrosive media and accelerate the corrosion process [21,22]. Therefore, for improved and advanced industrial applications such as cutting tool and biomedical, a detailed understanding about coating defects and their influence on coating performance is very crucial.

Deposition parameters such as deposition time, substrate temperature and bias voltage are influential on the coating growth mechanism [16,23–27]. Therefore, these parameters could also affect the coating defect formation. In addition to that, chamber pressure also has strong influence on coating properties especially for reactive deposition processes [28–30].

This research was aimed to study the impact of chamber pressure on defect generation and the subsequent effect of defects on coating performance. Both the corrosion and tribological performances of CrN/NbN coatings (deposited by Arc or conventional magnetron sputtering techniques) have already been investigated [21,22,31,32]. The benefits of using HIPIMS over conventional PVD to deposit CrN/NbN have been also demonstrated [16,33,34]. However, the impact of defects on the coating performance of HIPIMS deposited CrN/NbN was understudied and so far, very little attention was given towards the coatings defects associated with HIPIMS. These two reasons were the inspiration for the present work.

2. Experimental Details

2.1 Coating deposition:

An industrial sized (1 m^3) Hauzer 1000 four cathode PVD machine enabled with HIPIMS power supplies (Hüttinger Elektronik Sp. z o.o., Warsaw, Poland) and an advanced bias power supply (with active arc suppression units on cathode and substrate bias supplies) was used to deposit CrN/NbN nano-structured multilayer coatings. The deposition system was furnished with two Chromium (Cr) and two Niobium (Nb) targets (sized 600 x 200 mm). To enhance the adhesion of the coating with the substrate, HIPIMS plasma discharge enriched with Cr ions was used to pre-treat the surfaces of the substrate before coating deposition [35].

While depositing the coatings, UBM-DC was combined with HIPIMS to achieve a higher deposition rate [15]. All multilayer CrN/NbN coatings were produced by operating one Cr and one Nb target in HIPIMS mode and the other two targets (1 Cr and 1 Nb) in UBM mode. The machine was operated in constant power mode and the average power on the individual cathode was maintained at 8 kW irrespective of the technology (UBM or HIPIMS). Rectangular pulses of 200 µs at a frequency of 100 Hz, with a duty cycle of 1 % were employed to generate the HIPIMS plasma for coating deposition. During depositions, Ar and N_2 (1:1) were used as the process gas. Three sets of coatings were deposited at chamber pressures of 0.2 Pa, 0.35 Pa and 1 Pa. The bias voltage was fixed at - 65 V, the temperature was maintained at 200 °C and the deposition time was 120 min for all the coatings. To produce homogeneous coatings, samples were mounted onto a three-fold rotational substrate holder. The distance between the substrate holder and the cathodes was 0.2 m. 304 stainless steel coupons, M2 high speed steel coupons and (100) Silicon wafer were used as substrates.

2.2 Crystal structure study (XRD)

A PANalytical Empyrean PIXcel 3D automated diffractometer in glancing angle (GA) beam geometry was used to determine the crystal structure configuration. The scanning range for GA XRD was selected as $2\theta = 20°$ to $100°$ with a step size of $0.006°$ and the incident angle was fixed at $2°$. GA XRD is a convenient method for phase identification studies, due to the reduced penetration depth of the X-rays which eliminates the contribution related to the substrate in comparison to standard X-ray diffraction. The X-ray source used was monochromatic Cu-Kα radiation with a wavelength of 1.5406 nm. The voltage and current of the X-ray generation tube was 45 kV and 40 mA respectively. The Miller indices for all the phases present in the XRD patterns were calculated by X'Pert HighScore Plus Software.

2.3 Microstructural investigation

2.3.1. Scanning electron microscopy (FEI-Nova NanoSEM 200) was used to capture the secondary electron (SE) images of planar and fractural cross sectional view of the coatings. The working distance was in the range of 4 to 5 mm and the beam voltage was in the range of 5 to 20 kV in the process to capture clear images. These SEM images provided necessary information about coating thickness, morphology and defect structure. Energy-dispersive X-ray (EDX) analysis (OXFORD Instruments Aztec software) incorporated on the SEM was used to assess the chemical composition of the coating.

2.3.2. Huvitz 3D optical microscope and ImageJ software were used to analyse the percentage of surface area of the sample covered by the imperfections (i.e. the defect density in the coating). The images of the coating surfaces (130 µm × 90 µm) were captured using a digital camera attached with the microscope. The defect density was then quantified from binary pictures of the coatings [16]. This study was conducted to determine the effect of the chamber pressure on defect formation.

2.4 Electrochemical corrosion test

The corrosion behaviour of the CrN/NbN coating was examined using a Gill AC Potentiostat. At room temperature of 25 °C, all the electrochemical experiments were conducted by polarising the sample from - 1000 mV to + 1000 mV at a scan rate of 0.5 mV per sec in a 3.5 % NaCl solution. During the test, the exposed surface area of the CrN/NbN coated 304 stainless steel sample was 1 cm^2. These measurements were aimed at studying the role of defects on the corrosion resistance of the coatings.

2.5 Pin-on-disc tribology test

To study the friction behaviour of the deposited coatings in dry sliding conditions a CSM room temperature pin-on-disc tribometer was used. CrN/NbN coated M2 high speed steel samples were used for this test with Al_2O_3 balls of 6 mm diameter used as a counterpart. For all the experiments, the number of laps was fixed at 20000 and 5 N static load was applied to measure friction rates. The room temperature and the relative humidity during the experiments were 25 °C and 15 % respectively. After the test, the wear coefficient (K_C) was calculated using Archard's equation as $K_C = V/F_N \times d$, where V is wear volume in m^3, F_N is normal load in Newtons and d is the sliding distance in meters. The wear volume V was calculated as $V = 2\pi RA$, where R stands for wear track radius and A is cross-sectional area of the wear track. A Veeco Dektak 150 surface profilometer was used to measure the radius (R) and the cross-sectional area (A) of the wear track after the test.

2.8 Raman spectroscopy

Raman spectroscopy was used to investigate the chemistry of the tribolayer formed during sliding. A Horiba-Jobin-Yvon LabRam HR800 integrated Raman spectrometer fitted with a green laser (wavelength 532 nm) was used to collect the Raman spectra of the wear track and

wear debris. To reduce the intensity of incident beam and to avoid irradiation damage, a 10 % transmission filter was applied.

3. Results & Discussion

3.1 Measurement of the coating thickness and deposition rate

Fig. 1 shows the variation of the coating thickness as a function of chamber pressure. To determine the influence of chamber pressure on deposition rate, the thickness of the coatings was measured by SEM using fracture cross-sections of the coating deposited on Si wafer.

The graph shows that the thickest coating (3.65 µm) was produced at the lowest chamber pressure (0.2 Pa). The thickness then decreased suddenly to 2.15 µm with the increase of chamber pressure to 0.35 Pa. The most likely reason for decreasing thickness may be the strong resputtering of the depositing materials at very high pressure. Also, the diffusive collisions of depositing species within the plasma and the target poisoning can decrease the deposition rate [30,36]. For reactive sputtering, target poisoning is a very common phenomenon [37]. Although, during these coating depositions, N_2 and Ar flow rates (sccm) were fixed (always 1:1); but a slight increase in the ratio of the partial pressures of N_2 and Ar with the increase of the chamber pressure was observed. The ratio P_{N_2} / P_{Ar} was varied from 0.85 at 0.2 Pa to 0.95 at 1 Pa. The change in the partial pressures could slightly increase the target poisoning at higher chamber pressures. Due to the formation of nitride layers on the target surfaces the sputter rate was reduced. Nevertheless, the mean free paths (λ) of the plasma species (neutral atoms, ions) were also reduced with the increase of chamber pressure. The reactive gas (Ar + N_2) atmosphere during HIPIMS process is highly ionised [38] which makes the kinetics of the atoms/ions extremely complex. However, assuming the plasma atmosphere similar to the ideal gas atmosphere, the mean free paths at different chamber pressure were calculated (using Van der Waals radius (R) of Nitrogen = 1.55×10^{-10} m). At

0.2 Pa chamber pressure, the λ value was found to be 0.11 m. The λ value then decreased to 0.06 m at P = 0.35 Pa and 0.02 m at P = 1 Pa. This calculation clearly indicated that the collision frequency was higher at higher chamber pressures which decreased the possibility of sputtered species to reach the substrates directly without colliding with the gas species. Thus, the decrease in deposition rate at higher chamber pressure could be attributed to the combined effect of target poisoning and resputtering & diffusive collision of depositing materials.

3.2 Crystallographic structure

GA XRD patterns of the CrN/NbN superlattice coatings are shown in Fig. 2. This measurement revealed that the crystal structures of nanoscale CrN/NbN coatings were of a single phase fcc lattice. The coating deposited at the lowest chamber pressure of 0.2 Pa displayed a pronounced (200) orientation of the nitride phase. With the increase of chamber pressure to 0.35 Pa, the preferred orientation was shifted from (200) to (111). For the highest chamber pressure of 1 Pa, the preferred orientation again changed to (200). Similar behaviour was observed for CrN coatings when the nitrogen percentage was varied [39]. The change in the nitrogen volume within the chamber, resputtering of the depositing materials and different deposition rates of Cr and Nb at different chamber pressures can cause the variation between the chromium nitride and niobium nitride layers in the structure [40]. As a result, the crystallographic orientation of the coatings was changed. One satellite peak (SP) is visible at the left sides of the (200) for the coating deposited at P = 0.2 Pa which indicated good coating crystallinity and good chemical modulation of the coating [32].

3.3. Microstructural study of coating defects

SEM was used to study the coating morphology and microstructure. High magnified planar and fracture cross sectional SEM images of the coatings revealed the existence of four types

of defects (Fig. 3a-d). Depending on their growth mechanism and structure, the defects were categorised as nodular, open void defects, cone-like and pinhole defects [17].

Among these four types of defects, nodular, open void and cone-like defects are associated with dust particles, flakes coming from the chamber components. A fourth types of defects are called pinhole defects (Fig. 3d) which generate due to the pre-existence of substrate pits. Detailed study about these defects can be found elsewhere [16,41].

3.4. Defect density calculation by Optical Microscopy and Image J software

Fig. 4a shows the surface of the deposited coatings captured by optical microscope and Fig. 4b represents the converted binary image of the same surface.

The relationship of defect density (percentage of area covered by defects) with the chamber pressure is shown in Fig. 5.

As seen in the figure, the defect density increased from 0.84 % to 5.94 % with increase of the chamber pressure from 0.2 Pa to 1 Pa. The increase in defect density was associated with the increase in flake generation. At the higher chamber pressure, plasma volume covers more area of the chamber, which can increase the amount of sputter flux bombardments on chamber wall and subsequent flake generation. These flakes can initiate more defect sites and cause further defect formation within the coating. In addition to that, intense resputtering at higher chamber pressure can reveal loosely bound defects more and increase the area associated with the defects.

This study was conducted in a chamber which was not cleaned before or between two subsequent coating deposition processes. For this reason, this result is interesting because it clearly shows that the chamber pressure can be used as an effective tool to control the defect density, even in an industrial environment where it is not possible to thoroughly clean an industrial sized chamber frequently.

3.5 Electrochemical corrosion test

Previous studies have suggested that the corrosion properties of multilayer PVD coatings depend on their chemical composition, stress level, porosity and thickness as well as on the morphological defects of the coatings [7,16,20–22,34]. To study the effect of the defects on corrosion performance of CrN/NbN nano-scale multilayer coatings, electrochemical corrosion tests were conducted.

Fig. 6 shows the potentiodynamic polarisation curves of CrN/NbN coatings deposited by varying the chamber pressures. In the potential range of - 300 mV to + 300 mV, the corrosion current density was significantly higher for the coating produced at the highest chamber pressure (1 Pa). Thicknesses of the coatings deposited at 0.35 Pa and 1 Pa chamber pressure were almost the same (2.15 μm and 2.18 μm); however defect density was higher (5.96 %) for the coating deposited at 1 Pa pressure. These increased defects are believed to be the reason for lower corrosion resistance. The thickest coating (3.65 μm) with the lowest defect density, (0.84 %) was produced at the lowest chamber pressure (0.2 Pa). For this coating, pitting resistance was more evident (in the potential range of - 300 mV to + 300 mV). This study confirmed the deleterious effect of coating defects on corrosion performance.

3.6. Tribological properties

The wear and friction behaviour of CrN/NbN coatings were evaluated by pin on disc tests in dry sliding conditions. The friction co-efficient i.e, COF (μ) of CrN/NbN coatings against number of laps has been plotted in Fig. 7. Whereas, Fig. 8 shows the wear tracks of the coatings deposited by varying chamber pressure.

The coatings deposited at the higher pressures of 0.35 Pa and 1 Pa, had the higher number of surface defects. As observed in the friction curve, the coatings deposited at higher pressures exhibited high noise, which is typical of a sliding wear process with a large amount of debris

involved in a three-body rolling contact mechanism [42]. Due to the friction between the alumina ball and coating surfaces, loosely bonded defects could be expunged and these defects can increase the wear debris formation during the tribological tests. Thus, the noise was more pronounced for the coatings with higher defects.

The coating deposited at 0.2 Pa, had the lowest defect density (0.84 %) and the coating deposited at 1 Pa had the highest defect density (5.96 %) but both the coatings showed similar friction co-efficient (μ = 0.69 and 0.70 respectively) and wear co-efficient ($K_c = 1.6 \times 10^{-15}$ $m^3N^{-1}m^{-1}$ and 1.7×10^{-15} $m^3N^{-1}m^{-1}$ respectively) values.

To understand the tribological properties of these coatings, the influence of the chamber pressure on crystallographic orientation was studied. It is well known that crystallographic orientation influences tribological behaviour of the coatings [43–46]. In addition, Raman spectra were obtained from the corresponding wear track and wear debris of the CrN/NbN coatings to evaluate the nature of the oxides produced at the tribological contact.

Fig. 9 shows the variation of wear co-efficient and peak intensity ratio with the chamber pressure. It is clear from the figure that the crystallographic orientation directly influenced the wear rate of the coatings. The coating with (111) preferred orientation had the highest wear rate (2.6×10^{-15} $m^3N^{-1}m^{-1}$) whereas (200) oriented coatings had the lowest wear rates ($K_c = 1.6 \times 10^{-15}$ $m^3N^{-1}m^{-1}$ and 1.7×10^{-15} $m^3N^{-1}m^{-1}$).

The friction behaviour was influenced by the type of oxides formed during the tests. As obtained from the Raman study (Fig. 10), the tribolayer produced on the coatings deposited at chamber pressures of 0.2 Pa and 1 Pa had pronounced peaks at around 535 cm^{-1} (corresponds to Cr_2O_3) and 840 cm^{-1} (corresponds to Nb_2O_5, nH_2O) [47,48]. Cr_2O_3 belongs to the family of magneli phases and therefore it is more lubricious [49]. In contrast, Nb_2O_5 has a crystallographic structure which does not contain easily shearable atomic planes and

therefore it is less lubricious. Thus the higher friction co-efficient of these coatings can be attributed to the presence of Nb_2O_5 in the tribolayer. The coating deposited at 0.35 Pa chamber pressure showed only one peak at around 625 cm^{-1} (corresponds to $CrNbO_4$). This coating however, showed the lowest friction co-efficient value, 0.48. This $CrNbO_4$ based tribolayer must have a lower co-efficient of friction compared to the tribolayer formed on the top the coatings deposited at 0.2 Pa and 1 Pa.

As discussed above, the effect of defects on friction properties was not clearly evident. However, a number of publications have shown the influence of defects on the tribological properties of the coatings [18,19]. So an additional study was conducted. A set of coatings was produced at 0.35 Pa after the chamber parts were cleaned. As the origin of most defects were flakes (discussed in the section 3.3, 3.4), the defect density of the coating produced in a clean chamber reduced by almost three times from 3.18 % before cleaning to 1.37 % after cleaning.

Fig. 11 shows the friction curves of the coatings (deposited at 0.35 Pa) with different defect densities. As observed, the friction co-efficient (μ) reduced by a factor of two from 0.48 to 0.25 when the defect density decreased from 3.18 % to 1.37 %.

To study the effect of the tribolayer on the friction behaviour of this coating (P = 0.35 Pa and defect density = 1.37 %), Raman spectra were taken. As shown in the Fig. 12, the Raman spectra of the tribolayer were similar for both the coatings deposited at 0.35 Pa chamber pressure. This emphasised the fact that the difference in the friction behaviour of these coatings is clearly due to the defect density rather than the chemistry of the tribolayer formed in the wear track.

Conclusion:

CrN/NbN multilayer coatings were deposited by varying the chamber pressure to study the effect of chamber pressure on defect formation as well as to understand the influence of these defects on coating corrosion and tribological properties. Defect density calculations confirmed that the defect density of the coating was directly influenced by the chamber pressure. Coatings produced at the lowest chamber pressure (0.2 Pa) had the lowest defect density (0.84 %). The exclusive study on these defects revealed that external factors such as flakes and pre-existing substrate pits initiated these defects' formation.

The Potentiodynamic polarisation study confirmed that the defect density dominated the coating corrosion behaviour. The coating with the highest defect density (5.96 %) had the lowest E_{corr} value (-313 mV). Also, in the potential range from - 300 mV to + 300 mV, the corrosion current density of this coating was significantly higher compared to the coatings with fewer defects (0.84 % and 3.17 %). This result clearly indicated that the coating with the highest defect density had the lowest corrosion resistance.

The tribological properties were influenced by the oxides formed at tribological contact as well as the crystallographic orientation of the coating. Coatings with (200) crystallographic orientation (deposited at 0.2 Pa and 1 Pa) had lower wear rates (~1.6×10^{-15} $m^3N^{-1}m^{-1}$) whereas coating with (111) crystallographic orientation (deposited at 0.35 Pa) had the highest wear rate (2.6×10^{-15} $m^3N^{-1}m^{-1}$). Friction behaviour of these coatings was more influenced by the nature of oxides formed at the tribological contacts. The coating deposited at 0.35 Pa had the lowest friction co-efficient ($\mu = 0.48$). Raman spectra of the tribolayer formed on the top of this coating suggested that it contained $CrNbO_4$. In contrast, a Nb_2O_5 based tribolayer in the wear track was formed for the coatings deposited at 0.2 Pa and 1 Pa. Both these coatings

showed higher friction values (μ = 0.69 and 0.70 respectively) because of the non-lubricious nature of the niobium oxides.

An additional study was conducted to understand the influence of defect density on tribological properties of the coatings. One set of coatings was produced in a relatively clean chamber at a chamber pressure of 0.35 Pa. As expected, defect density reduced to 1.37 % as compared to 3.18 % before cleaning. The pin-on-disk tribological tests showed that the friction co-efficient (μ) reduced from 0.48 to 0.25 with the decrease in defect density. This additional study confirmed that along with the crystallographic orientation and the oxides formed at tribological contact, defect density plays a major role in the tribological performance of the coatings.

Acknowledgement

This study was carried out within a PhD research programme. The financial support by Zimmer-Biomet (E12093B/JS/BB) is gratefully acknowledged.

Reference:

[1] E. Roliński, Surface properties of plasma-nitrided titanium alloys, Mater. Sci. Eng. A. 108 (1989) 37–44. doi:10.1016/0921-5093(89)90404-8.

[2] M.Y. Wee, Y.G. Park, T.S. Kim, Surface properties of CrN-coated Ti-6Al-4V alloys by arc-ion plating process, Mater. Lett. 59 (2005) 876–879. doi:10.1016/j.matlet.2004.11.035.

[3] H.C. Barshilia, K.S. Rajam, A. Jain, K. Gopinadhan, S. Chaudhary, A comparative study on the structure and properties of nanolayered TiN/NbN and TiAlN/TiN multilayer coatings prepared by reactive direct current magnetron sputtering, Thin Solid Films. 503 (2006) 158–166. doi:10.1016/j.tsf.2005.12.074.

[4] U. Helmersson, S. Todorova, S.A. Barnett, J.E. Sundgren, L.C. Markert, J.E. Greene, Growth of single-crystal TiN/VN strained-layer superlattices with extremely high mechanical hardness, J. Appl. Phys. 62 (1987) 481–484. doi:10.1063/1.339770.

[5] M. Larsson, P. Hollman, P. Hedenqvist, S. Hogmark, U. Wahlström, L. Hultman, Deposition and microstructure of PVD TiN-NbN multilayered coatings by combined reactive electron beam evaporation and DC sputtering, Surf. Coatings Technol. 86–87 (1996) 351–356. doi:10.1016/S0257-8972(96)03026-5.

[6] M. Nordin, M. Herranen, S. Hogmark, Influence of lamellae thickness on the corrosion behaviour of multilayered PVD TiN/CrN coatings, Thin Solid Films. 348 (1999) 202–209. doi:10.1016/S0040-6090(99)00192-3.

[7] M. Tomlinson, S.B. Lyon, P. Hovsepian, W.D. Munz, Corrosion performance of CrN/NbN superlattice coatings deposited by the combined cathodic arc/unbalanced magnetron technique, Vacuum. 53 (1999) 117–121. doi:10.1016/S0042-207X(98)00405-9.

[8] M. Lattemann, A.P. Ehiasarian, J. Bohlmark, P.Å.O. Persson, U. Helmersson, Investigation of high power impulse magnetron sputtering pretreated interfaces for adhesion enhancement of hard coatings on steel, Surf. Coatings Technol. 200 (2006) 6495–6499. doi:10.1016/j.surfcoat.2005.11.082.

[9] J. Lin, J.J. Moore, W.D. Sproul, B. Mishra, J.A. Rees, Z. Wu, R. Chistyakov, B. Abraham, Ion energy and mass distributions of the plasma during modulated pulse power magnetron sputtering, Surf. Coatings Technol. 203 (2009) 3676–3685. doi:10.1016/j.surfcoat.2009.05.048.

[10] A.P. Ehiasarian, Fundamentals and applications of HIPIMS, R. Wei (Ed.), Plasma Surf. Eng. Res. Its. Pract. Appl. Res. Signpost, Trivandrum, India, 2008: pp. 35–86.

[11] J. Alami, P.O.Å. Persson, D. Music, J.T. Gudmundsson, J. Bohlmark, U. Helmersson, Ion-assisted physical vapor deposition for enhanced film properties on nonflat surfaces, J. Vac. Sci. Technol. A Vacuum, Surfaces, Film. 23 (2005) 278–280. doi:10.1116/1.1861049.

[12] Q. Ma, L. Li, Y. Xu, J. Gu, L. Wang, Y. Xu, Effect of bias voltage on TiAlSiN nanocomposite coatings deposited by HiPIMS, Appl. Surf. Sci. 392 (2017) 826–833. doi:10.1016/j.apsusc.2016.09.028.

[13] H. Hoche, S. Groß, M. Oechsner, Development of new PVD coatings for magnesium alloys with improved corrosion properties, Surf. Coatings Technol. 259 (2014) 102–108. doi:10.1016/j.surfcoat.2014.04.038.

[14] J. Lin, J.J. Moore, W.D. Sproul, B. Mishra, Z. Wu, J. Wang, The structure and properties of chromium nitride coatings deposited using dc, pulsed dc and modulated pulse power magnetron sputtering, Surf. Coatings Technol. 204 (2010) 2230–2239. doi:10.1016/j.surfcoat.2009.12.013.

[15] P.E. Hovsepian, A.A. Sugumaran, Y. Purandare, D.A.L. Loch, A.P. Ehiasarian, Effect of the degree of high power impulse magnetron sputtering utilisation on the structure and properties of TiN films, Thin Solid Films. 562 (2014) 132–139. doi:10.1016/j.tsf.2014.04.002.

[16] B. Biswas, Y. Purandare, A.A. Sugumaran, D.A.L. Loch, S. Creasey, A.P. Ehiasarian, P.E. Hovsepian, I. Khan, Defect growth in multilayer chromium nitride/niobium nitride coatings produced by combined high power impulse magnetron sputtering and unbalance magnetron sputtering technique, Thin Solid Films. 636 (2017) 558–566. doi:10.1016/j.tsf.2017.06.027.

[17] P. Panjan, M. Čekada, M. Panjan, D. Kek-Merl, Growth defects in PVD hard coatings, Vacuum. 84 (2009) 209–214. doi:10.1016/j.vacuum.2009.05.018.

[18] A. Drnovšek, P. Panjan, M. Panjan, M. Čekada, The influence of growth defects in

sputter-deposited TiAlN hard coatings on their tribological behavior, Surf. Coatings Technol. 288 (2016) 171–178. doi:10.1016/j.surfcoat.2016.01.021.

[19] M. Tkadletz, C. Mitterer, B. Sartory, I. Letofsky-Papst, C. Czettl, C. Michotte, The effect of droplets in arc evaporated TiAlTaN hard coatings on the wear behavior, Surf. Coatings Technol. 257 (2014) 95–101. doi:10.1016/j.surfcoat.2014.01.010.

[20] S. Creasey, D.B. Lewis, I.J. Smith, W.-D. Münz, SEM image analysis of droplet formation during metal ion etching by a steered arc discharge, Surf. Coatings Technol. 97 (1997) 163–175. doi:10.1016/S0257-8972(97)00137-0.

[21] H.W. Wang, M.M. Stack, S.B. Lyon, P. Hovsepian, W.D. Münz, The corrosion behaviour of macroparticle defects in arc bond-sputtered CrN/NbN superlattice coatings, Surf. Coatings Technol. 126 (2000) 279–287. doi:10.1016/S0257-8972(00)00554-5.

[22] D.B. Lewis, S.J. Creasey, C. Wustefeld, A.P. Ehiasarian, P.E. Hovsepian, The role of the growth defects on the corrosion resistance of CrN/NbN superlattice coatings deposited at low temperatures, Thin Solid Films. 503 (2006) 143–148. doi:10.1016/j.tsf.2005.08.375.

[23] V. Vasanthipillay, K. Vijayalakshmi, Influence of Sputter Deposition Time on the Growth of c-Axis Oriented AlN / Si Thin Films for Microelectronic Application, 2012 (2012) 724–729.

[24] D. Bhaduri, A. Ghosh, S. Gangopadhyay, S. Paul, Effect of target frequency, bias voltage and bias frequency on microstructure and mechanical properties of pulsed DC CFUBM sputtered TiN coating, Surf. Coatings Technol. 204 (2010) 3684–3697. doi:10.1016/j.surfcoat.2010.04.047.

[25] S. Gangopadhyay, R. Acharya, A.K. Chattopadhyay, S. Paul, Effect of substrate bias voltage on structural and mechanical properties of pulsed DC magnetron sputtered TiN-MoSx composite coatings, Vacuum. 84 (2010) 843–850. doi:10.1016/j.vacuum.2009.11.010.

[26] J.-W. Lee, S.-K. Tien, Y.-C. Kuo, C.-M. Chen, The mechanical properties evaluation of the CrN coatings deposited by the pulsed DC reactive magnetron sputtering, Surf. Coatings Technol. 200 (2006) 3330–3335. doi:10.1016/j.surfcoat.2005.07.047.

[27] H. Du, J. Xiong, H. Zhao, Y. Wu, W. Wan, L. Wang, Structure and properties of TiAlLaN films deposited at various bias voltages, Appl. Surf. Sci. 292 (2014) 688–694. doi:10.1016/j.apsusc.2013.12.035.

[28] E. Penilla, J. Wang, Pressure and Temperature Effects on Stoichiometry and Microstructure of Nitrogen-Rich TiN Thin Films Synthesized via Reactive Magnetron DC-Sputtering, J. Nanomater. 2008 (2008) 1–9. doi:10.1155/2008/267161.

[29] L. Shan, Y. Wang, J. Li, J. Chen, Effect of N2 flow rate on microstructure and mechanical properties of PVD CrNx coatings for tribological application in seawater, Surf. Coatings Technol. 242 (2014) 74–82. doi:10.1016/j.surfcoat.2014.01.021.

[30] T. Shimizu, H. Komiya, Y. Teranishi, K. Morikawa, H. Nagasaka, M. Yang, Pressure dependence of (Ti, Al)N film growth on inner walls of small holes in high-power impulse magnetron sputtering, Thin Solid Films. 624 (2017) 189–196. doi:10.1016/j.tsf.2016.09.041.

[31] R. Ramadoss, N. Kumar, S. Dash, D. Arivuoli, A.K. Tyagi, Wear mechanism of CrN/NbN superlattice coating sliding against various counterbodies, Int. J. Refract. Met. Hard Mater. 41 (2013) 547–552. doi:10.1016/j.ijrmhm.2013.07.005.

[32] J.A. Araujo, G.M. Araujo, R.M. Souza, A.P. Tschiptschin, Effect of periodicity on hardness and scratch resistance of CrN/NbN nanoscale multilayer coating deposited by cathodic arc technique, Wear. 330–331 (2015) 469–477. doi:10.1016/j.wear.2015.01.051.

[33] Y.P. Purandare, A.P. Ehiasarian, M.M. Stack, P.E. Hovsepian, CrN/NbN coatings deposited by HIPIMS: A preliminary study of erosion-corrosion performance, Surf. Coatings Technol. 204 (2010) 1158–1162. doi:10.1016/j.surfcoat.2009.11.006.

[34] Y.P. Purandare, A.P. Ehiasarian, P.E. Hovsepian, Deposition of nanoscale multilayer CrN/NbN physical vapor deposition coatings by high power impulse magnetron sputtering, J. Vac. Sci. Technol. A Vacuum, Surfaces, Film. 26 (2008) 288–296. doi:10.1116/1.2839855.

[35] A.P. Ehiasarian, P.E. Hovsepian, W.-D. Münz, Combined coating process comprising magnetic field-assisted, high-power, pulsed cathode sputtering and an unbalanced magnetron, Patent US7081186 B2 (25 Jul 2006), EP1260603 A2 (27 Nov 2002), DE10124749 A1 (28 Nov 2002).

[36] Y.P. Purandare, A.P. Ehiasarian, P. Eh Hovsepian, Target poisoning during CrN deposition by mixed high power impulse magnetron sputtering and unbalanced magnetron sputtering technique, J. Vac. Sci. Technol. A Vacuum, Surfaces, Film. 34 (2016) 41502. doi:10.1116/1.4950886.

[37] D. Depla, R. De Gryse, Target poisoning during reactive magnetron sputtering: Part I: The influence of ion implantation, Surf. Coatings Technol. 183 (2004) 184–189. doi:10.1016/j.surfcoat.2003.10.006.

[38] A.P. Ehiasarian, Y.A. Gonzalvo, T.D. Whitmore, Time-resolved ionisation studies of the high power impulse magnetron discharge in mixed argon and nitrogen atmosphere, Plasma Process. Polym. 4 (2007) 309–313. doi:10.1002/ppap.200730806.

[39] Z.K. Chang, X.S. Wan, Z.L. Pei, J. Gong, C. Sun, Microstructure and mechanical properties of CrN coating deposited by arc ion plating on Ti6Al4V substrate, Surf. Coatings Technol. 205 (2011) 4690–4696. doi:10.1016/j.surfcoat.2011.04.037.

[40] D.C. Cameron, R. Aimo, Z.H. Wang, K.A. Pischow, Structural variations in CrN/NbN superlattices, Surf. Coatings Technol. 142 (2001) 567–572. doi:10.1016/S0257-8972(01)01057-X.

[41] P.E. Hovsepian, A.P. Ehiasarian, Y.P. Purandare, B. Biswas, F.J. Pérez, M.I. Lasanta, M.T. De Miguel, A. Illana, M. Juez-Lorenzo, R. Muelas, A. Agüero, Performance of HIPIMS deposited CrN/NbN nanostructured coatings exposed to 650°C in pure steam environment, Mater. Chem. Phys. 179 (2016) 110–119. doi:10.1016/j.matchemphys.2016.05.017.

[42] A.P. Ehiasarian, P.E. Hovsepian, L. Hultman, U. Helmersson, Comparison of microstructure and mechanical properties of chromium nitride-based coatings deposited by high power impulse magnetron sputtering and by the combined steered cathodic arc/unbalanced magnetron technique, Thin Solid Films. 457 (2004) 270–277. doi:10.1016/j.tsf.2003.11.113.

[43] S. Akkaya, B. Yıldız, M. Ürgen, Orientation dependent tribological behavior of TiN coatings., J. Phys. Condens. Matter. 28 (2016) 134009. doi:10.1088/0953-8984/28/13/134009.

[44] T. Wang, G. Zhang, B. Jiang, Comparison in mechanical and tribological properties of CrTiAlMoN and CrTiAlN nano-multilayer coatings deposited by magnetron sputtering, Appl. Surf. Sci. 363 (2016) 217–224. doi:10.1016/j.apsusc.2015.12.005.

[45] C. Tritremmel, R. Daniel, H. Rudigier, P. Polcik, C. Mitterer, Mechanical and tribological properties of Al-Ti-N/Al-Cr-B-N multilayer films synthesized by cathodic arc evaporation, Surf. Coatings Technol. 246 (2014) 57–63. doi:10.1016/j.surfcoat.2014.03.005.

[46] J. Lin, X. Zhang, Y. Ou, R. Wei, The structure, oxidation resistance, mechanical and tribological properties of CrTiAlN coatings, Surf. Coatings Technol. 277 (2015) 58–66. doi:10.1016/j.surfcoat.2015.07.013.

[47] J.H. Hsieh, C. Li, A.L.K. Tan, C.K. Poh, N.J. Tan, Study of oxidation and wear behaviors of (Nb,Cr)N thin films using Raman spectroscopy, Surf. Coatings Technol. 177–178 (2004) 299–305. doi:10.1016/j.surfcoat.2003.09.008.

[48] C.P. Constable, J. Yarwood, P. Hovsepian, L.A. Donohue, D.B. Lewis, W.-D. Münz, Structural determination of wear debris generated from sliding wear tests on ceramic coatings using Raman microscopy, J. Vac. Sci. Technol. A Vacuum, Surfaces, Film. 18 (2000) 1681–1689. doi:10.1116/1.582407.

[49] M.N. Gardos, Magn´ eli phases of anion-deficient rutile as lubricious oxides. Part I. Tribological behavior of single-crystal and polycrystalline rutile (TinO2n−1), Tribol. Lett. 8 (2000) 65–78. doi:10.1002/andp.200410099.

Figure Caption

Fig. 1. Variation of the coating thickness as a function of chamber pressure.

Fig. 2. GA XRD patterns of the coatings deposited by varying chamber pressure.

Fig. 3. (a) Cross sectional view of a nodular defect, (b) Cross sectional view of an open void defect, (c) cross section al view of a cone-like defect and (d) pinhole defects.

Fig. 4. (a) Optical microscopic image of coating surface and (b) Converted binary image of the same surface.

Fig. 5. Variation of coating defect density as a function of chamber pressure.

Fig. 6. Corrosion curves of the coatings deposited by varying chamber pressure.

Fig. 7. Friction curves of the coatings deposited by varying chamber pressure.

Fig. 8. Wear tracks of the coatings deposited by varying chamber pressure.

Fig. 9.Variation of wear co-efficient and peak intensity ratio with the chamber pressure.

Fig. 10. Raman spectra of the tribolayer produced on the coatings deposited by varying chamber pressure.

Fig. 11. Friction curves of the coatings (deposited at 0.35 Pa) with different defect density.

Fig. 12. Raman spectra of the tribolayers produced on the coatings (deposited at 0.35 Pa) with different defect density.

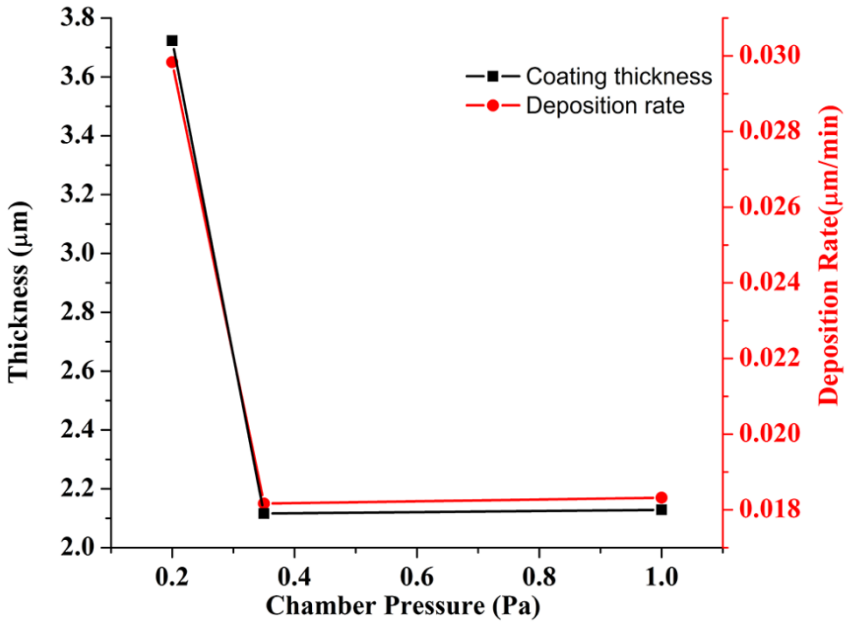

Fig. 1. Variation of the coating thickness as a function of chamber pressure.

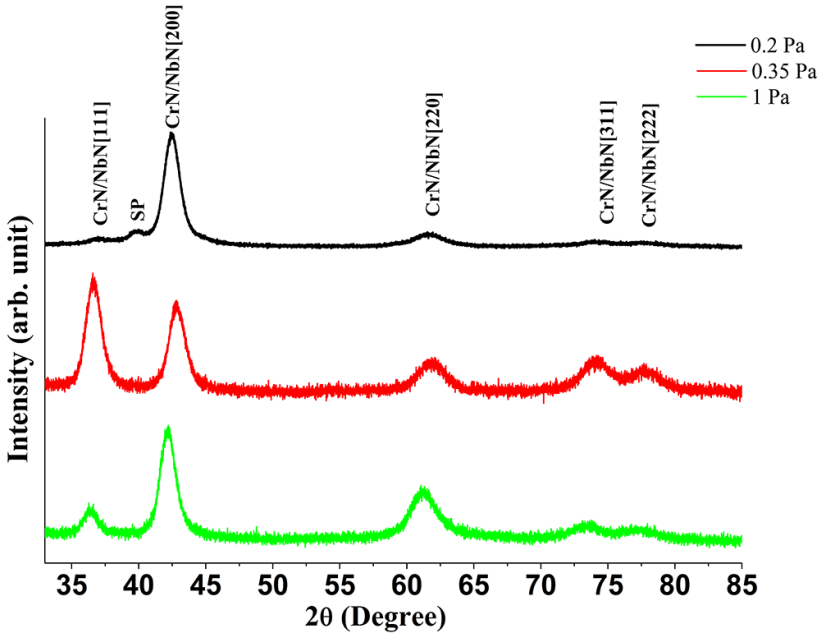

Fig. 2. GA XRD patterns of the coatings deposited by varying chamber pressure.

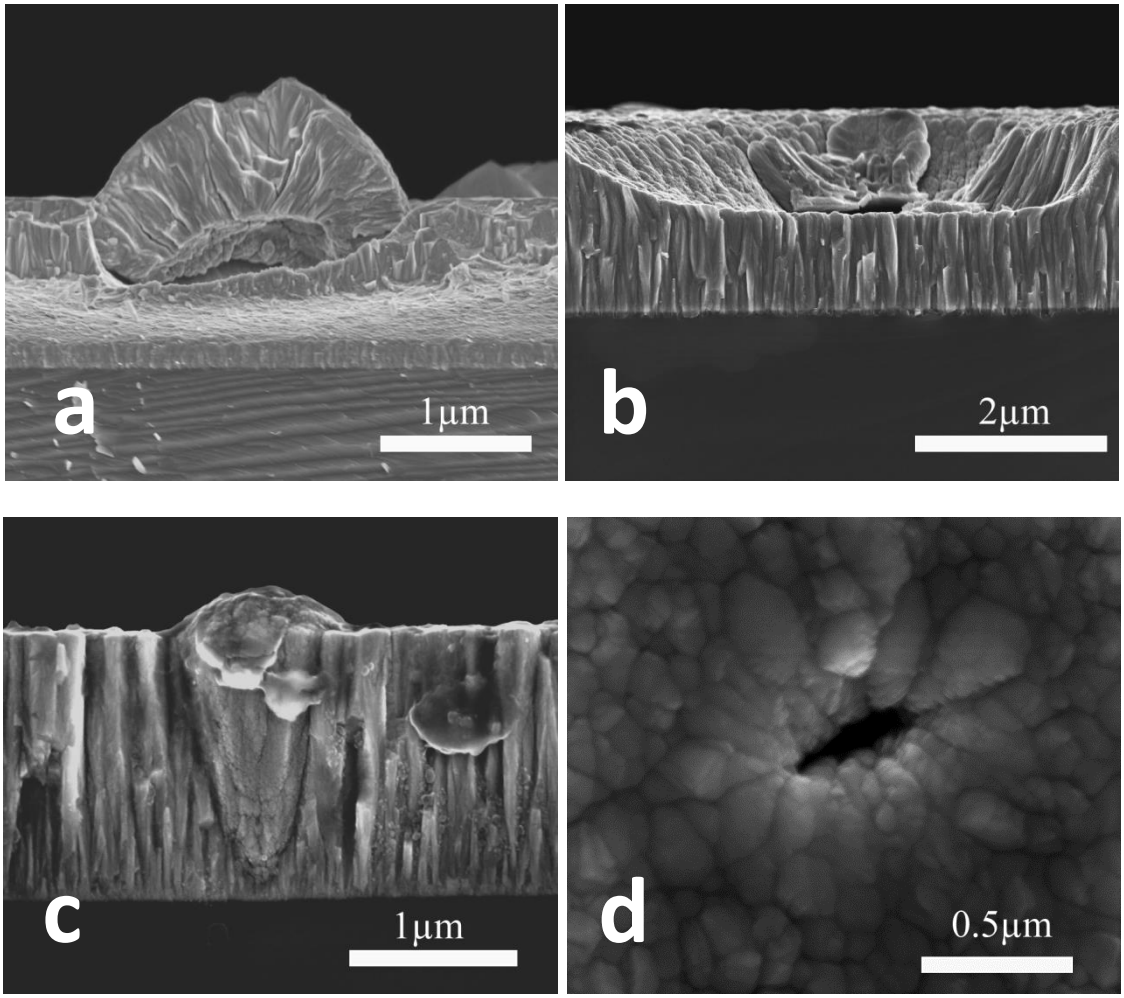

Fig. 3. (a) Cross sectional view of a nodular defect, (b) Cross sectional view of an open void defect, (c) cross section al view of a cone-like defect and (d) pinhole defects.

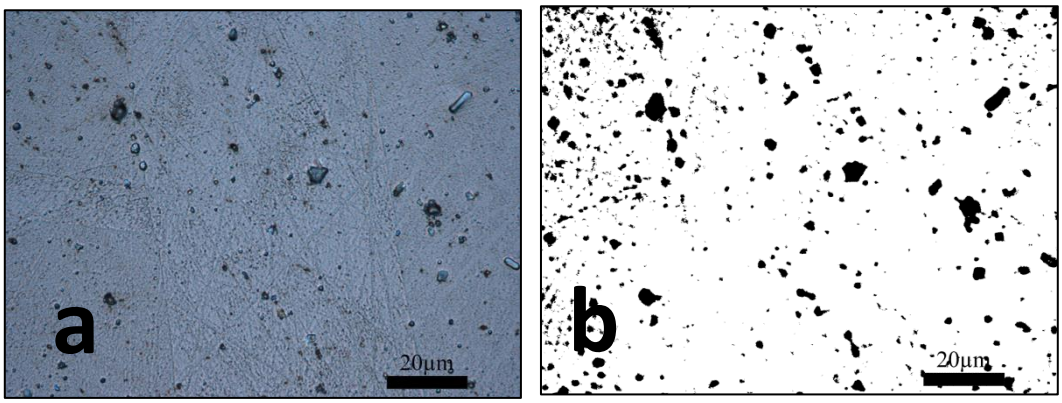

Fig. 4. (a) Optical microscopic image of coating surface and (b) Converted binary image of the same surface.

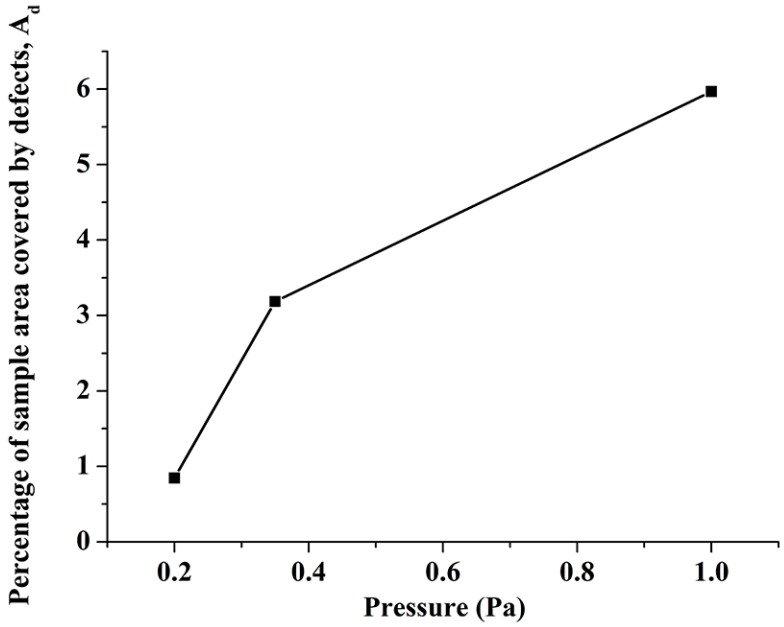

Fig. 5. Variation of coating defect density as a function of chamber pressure.

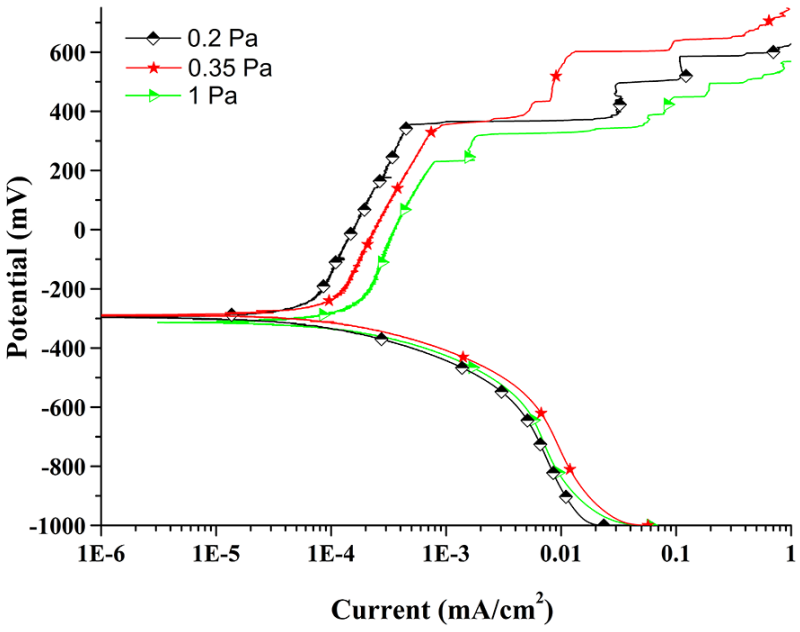

Fig. 6. Corrosion curves of the coatings deposited by varying chamber pressure.

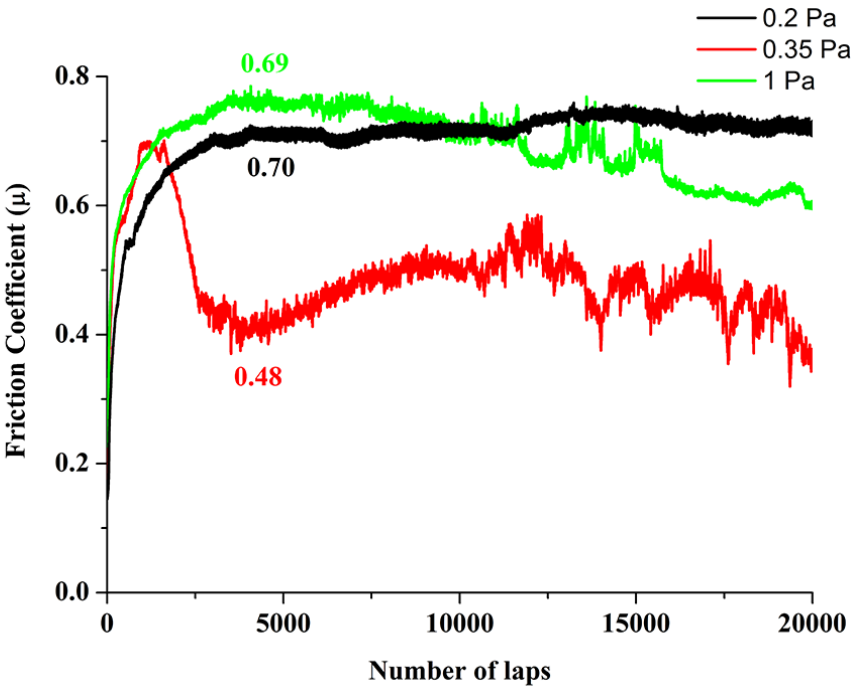

Fig. 7. Friction curves of the coatings deposited by varying chamber pressure.

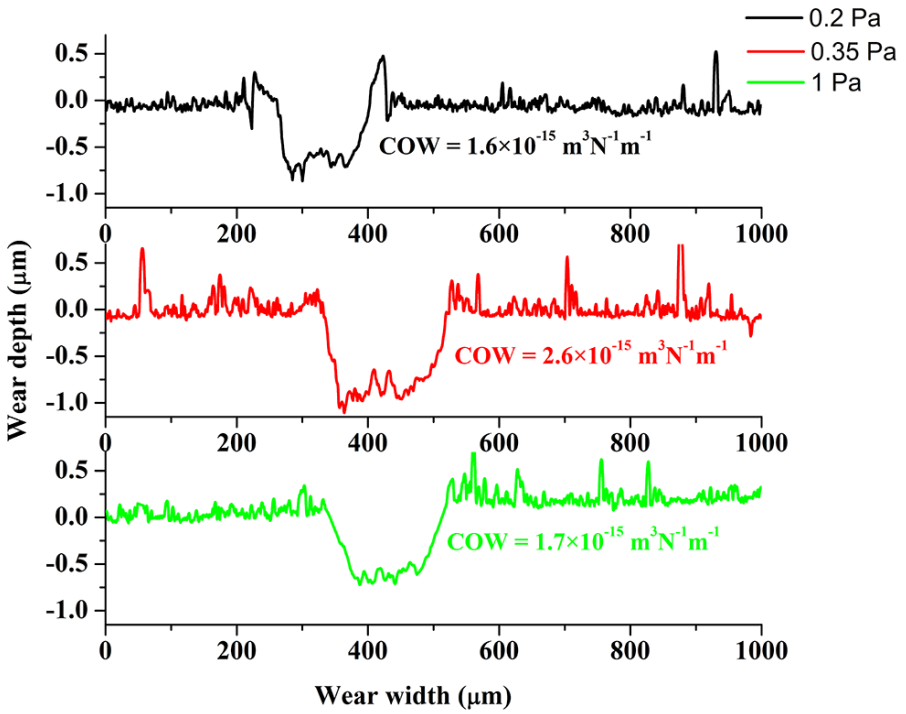

Fig. 8. Wear tracks of the coatings deposited by varying chamber pressure.

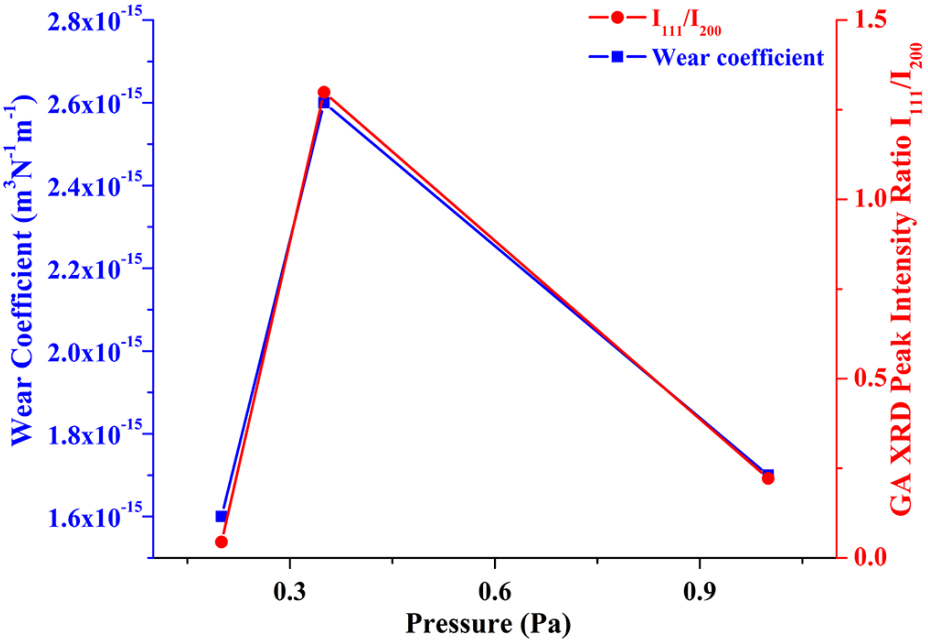

Fig. 9. Variation of wear co-efficient and peak intensity ratio with the chamber pressure.

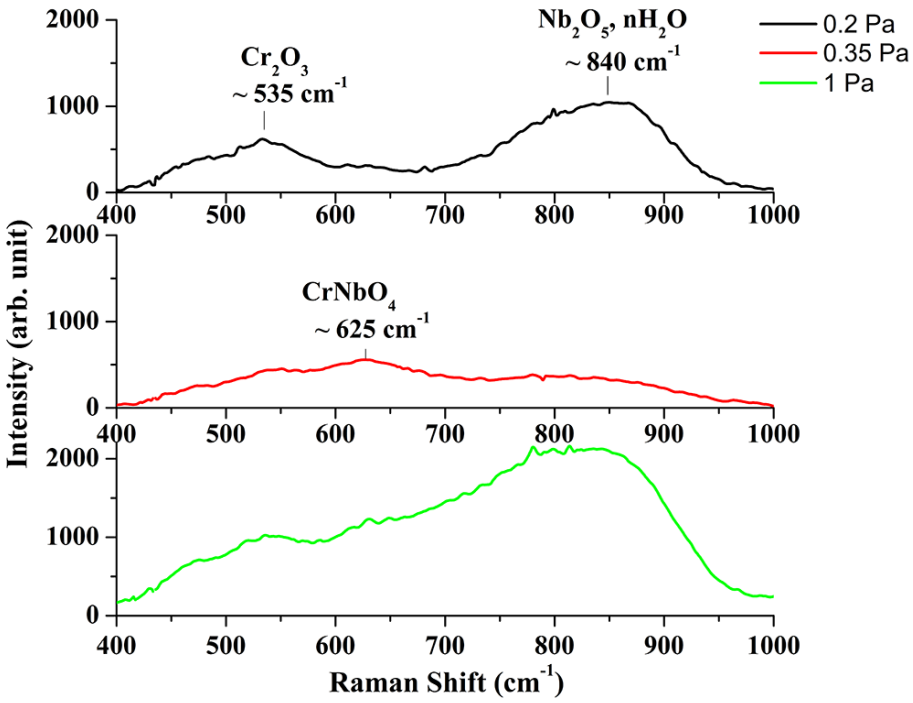

Fig. 10. Raman spectra of the tribolayer produced on the coatings deposited by varying chamber pressure.

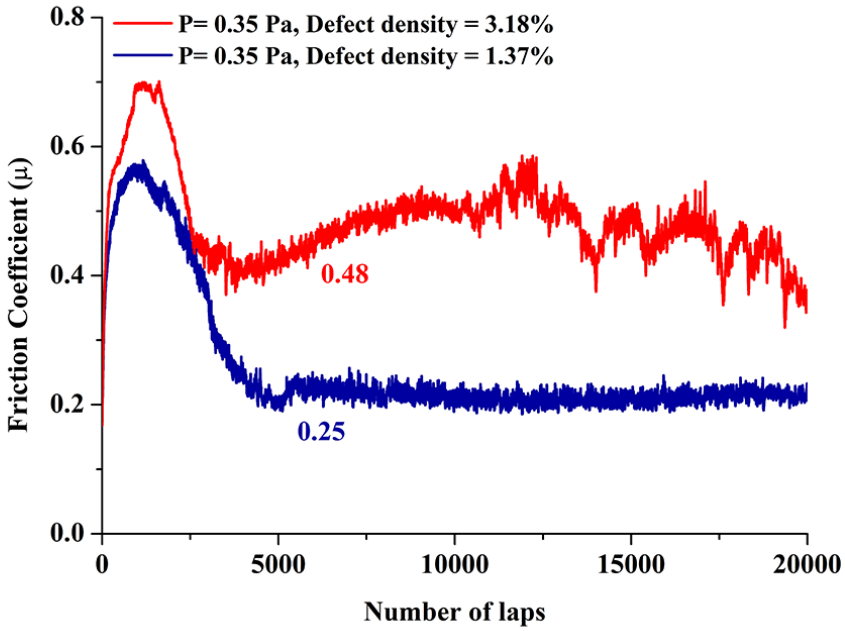

Fig. 11. Friction curves of the coatings (deposited at 0.35 Pa) with different defect density.

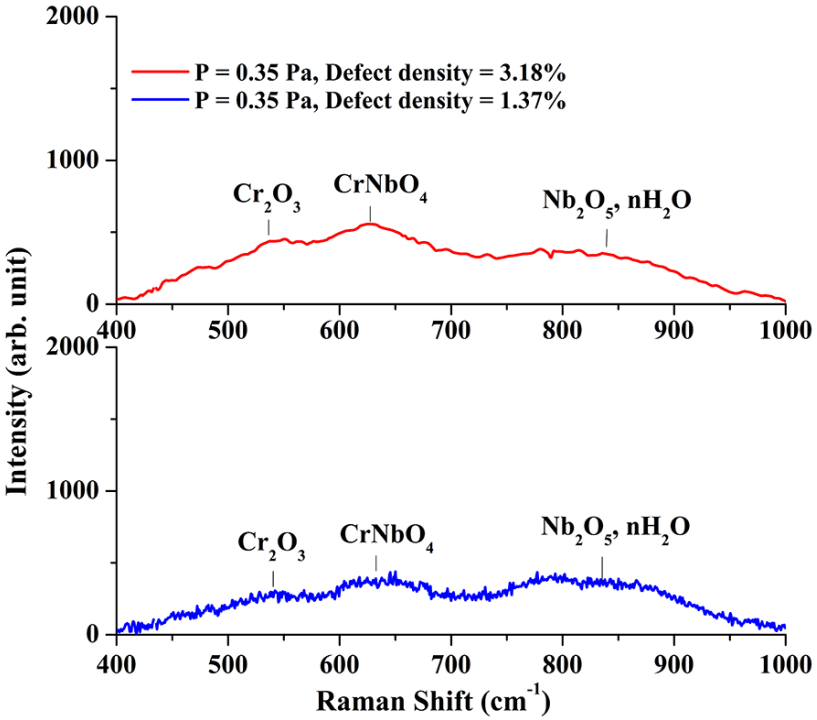

Fig. 12. Raman spectra of the tribolayers produced on the coatings (deposited at 0.35 Pa) with different defect density.